



Article

Steady-State Response Analysis of an Uncertain Rotor Based on Chebyshev Orthogonal Polynomials

Bensheng Xu ^{1,*}, Peijie Ning ^{1,†}, Guang Wang ¹ and Chaoping Zang ²

¹ School of Aeronautics, Guilin University of Aerospace Technology, Guilin 541004, China; ningpeijie@guat.edu.cn (P.N.); wangguang@mail.nwpu.edu.cn (G.W.)

² College of Energy and Power Engineering, Nanjing University of Aeronautics and Astronautics, Nanjing 210016, China; c.zang@nuaa.edu.cn

* Correspondence: xubensheng@guat.edu.cn

† These authors contributed equally to this work.

Abstract: The performance of a rotor system is influenced by various design parameters that are neither precise nor constant. Uncertainties in rotor operation arise from factors such as assembly errors, material defects, and wear. To obtain more reliable analytical results, it is essential to consider these uncertainties when evaluating rotor performance. In this paper, the Chebyshev interval method is employed to quantify the uncertainty in the steady-state response of the rotor system. To address the challenges of high-dimensional integration, an innovative sparse-grid integration method is introduced and demonstrated using a rotor tester. The effects of support stiffness, mass imbalance, and uncertainties in the installation phase angle on the steady-state response of the rotor system are analyzed individually, along with a comprehensive assessment of their combined effects. When compared to the Monte Carlo simulation (MCS) method and the full tensor product grid (FTG) method, the proposed method requires only 68% of the computational cost associated with MCS, while maintaining calculation accuracy. Additionally, sparse-grid integration reduces the computational cost by approximately 95.87% compared to the FTG method.

Keywords: uncertainty analysis; Chebyshev orthogonal polynomials; sparse-grid integration method; rotor system



Citation: Xu, B.; Ning, P.; Wang, G.; Zang, C. Steady-State Response Analysis of an Uncertain Rotor Based on Chebyshev Orthogonal Polynomials. *Appl. Sci.* **2024**, *14*, 10698. <https://doi.org/10.3390/app142210698>

Academic Editors: Yeyin Xu, Zhaobo Chen and Yingzhou Jiao

Received: 8 October 2024

Revised: 8 November 2024

Accepted: 15 November 2024

Published: 19 November 2024



Copyright: © 2024 by the authors. Licensee MDPI, Basel, Switzerland. This article is an open access article distributed under the terms and conditions of the Creative Commons Attribution (CC BY) license (<https://creativecommons.org/licenses/by/4.0/>).

1. Introduction

The rotor system is a vital component of rotating machinery such as aero engines and gas turbines. In the field of rotor dynamics, numerical simulators are commonly used to predict the dynamic behavior of the rotor system. However, uncertainties inherent in actual rotor systems stem from operational conditions and geometric parameters that may vary, including loose connections [1] or cracks [2]. These variations can lead to deviations from the expected steady-state response. Consequently, a steady-state response of the rotor system which initially meets design specifications may exceed acceptable limits in practice. A major challenge for engineers and researchers is to analyze and quantify the impacts of these uncertainties on the steady-state responses of complex rotor systems [3–5].

There are four commonly used methods for uncertainty analysis: the stochastic finite element method, probabilistic models, fuzzy methods, and interval methods. The stochastic finite element method assesses uncertainty by establishing stochastic differential equations for the system's response based on stochastic matrix theory or Taylor's formula [6]. Kureishi [7] applied this method to analyze a multi-degree-of-freedom rotor system in both time and frequency domains, investigating dynamics such as axial trajectory and random amplitude and frequency responses. Liu [8] developed a stochastic finite element model of a rotor-bearing system considering radial clearance randomness and employed the orthogonal polynomial method to examine the effects of factors like mean and coefficient of variation of radial clearances, eccentricity, and rotational speeds on the system's dynamic

performance. However, the stochastic finite element method's disadvantage is found in the difficulty and time consumed in deriving embedded equations when analyzing complex rotor systems. Probabilistic methods necessitate complete probability distributions of uncertain parameters, which are often challenging to obtain [9]. Fuzzy methods employ fuzzy variables to represent uncertain parameters, offering a robust framework for capturing the inherent ambiguity in a system's characteristics. The Fuzzy Stochastic Finite Element Method (FSFEM) is particularly advantageous, as it integrates fuzzy logic with stochastic modeling, allowing for a more comprehensive analysis of uncertainties in dynamic systems. Lara [10,11] utilized the FSFEM to investigate flexible rotor dynamics under uncertain parameters, examining the impacts of variables such as pad radius, oil viscosity, and radial clearance on tilting-pad journal bearings. However, the derivation of membership functions in fuzzy methods can be complex, presenting challenges when applied to the intricate task of rotor uncertainty analysis. Additionally, the effectiveness of the FSFEM may be limited by the presence of multi-source uncertainties, which complicates the modeling process and can hinder accurate assessments of system behavior.

Interval analysis is widely applied in uncertainty analysis. Although variations in system parameters are typically random, their range is usually finite, described as "unknown but bounded", indicating that the parameters fluctuate within definable intervals [12]. In the interval analysis of structural dynamics, uncertain parameters are represented as interval vectors, and differential equations governing rotor motion are formulated by incorporating these interval vectors. The solutions to these equations are derived using interval mathematics and regression theory, which facilitates the determination of the range of the system's steady-state response [13]. Ma [14,15] proposed a Bound Correction Interval Analysis Method (BCIM) based on Chebyshev expansion and modal superposition for the analysis of uncertain rotors. Mao [16] combined interval regression analysis with regularization to introduce a computational inverse method for identifying bearing loads. Utilizing interval analysis methods, Fu [17–19] examined the effects of uncertainties in several design parameters on rotors, including stiffness, damping, Young's modulus, cracking, and coupling misalignment. The interval analysis approach allows for the omission of specific probability distribution models for the uncertain parameters, requiring only the definition of their upper and lower fluctuation bounds. However, in scenarios characterized by multi-source uncertainty, this method necessitates the computation of combinations of specified integration points, such as Gaussian integration points, for multi-dimensional interval variables, thus significantly increasing the computational workload. To enhance computational efficiency, dimensionality reduction can be achieved through sparse generalized polynomial chaos expansion (gPCE) or polynomial dimensional decomposition [20–22]. Lu [23] employed a polynomial dimensional decomposition method to analyze the uncertainty in the response of a nonlinear rotor system, achieving effective dimensionality reduction. Nonetheless, when considering the nonlinear factors of the rotor system (e.g., nonlinear oil film damping), balancing computational efficiency and accuracy remains an area requiring further investigation.

The remainder of this paper is organized as follows: Section 2 presents the proposed methodology; this is followed by Section 3, which introduces an example of the research subject, namely a dynamically similar rotor tester for a turboshaft engine. Section 4 then discusses the results of the numerical analysis. Finally, Section 5 concludes the paper.

2. The Proposed Method

This section describes the method proposed in this paper, which encompasses both Chebyshev orthogonal polynomial approximation and the fundamental techniques of sparse-grid numerical integration. In the context of high-dimensional random variables, the use of sparse-grid numerical integration can effectively reduce computation time while maintaining calculation accuracy, thereby alleviating the "curse of dimensionality". To facilitate a clearer understanding, a flowchart is provided below for conducting uncertainty analysis of the steady-state response of rotor systems based on Chebyshev orthogonal polynomials.

2.1. Chebyshev Orthogonal Polynomial Approximation

Suppose $\xi = [\xi_1, \xi_2, \dots, \xi_n]$, ξ_j ($j = 1, \dots, n$) is a standard random variable with a uniform distribution $\mathcal{U}(-1, 1)$. Using the tensor product approach, an n -dimensional, k -order Chebyshev polynomial $T_{i_1, \dots, i_n}(\xi)$ can be defined as follows:

$$T_{i_1, \dots, i_n}(\xi) = \prod_{i_1 + \dots + i_n = k} T_{i_1}(\xi_1) \cdots T_{i_n}(\xi_n) \tag{1}$$

where i_1, i_2, \dots, i_n are non-negative integers. T_{i_j} denotes a Chebyshev polynomial with order i_j . For example, if $n = 2$, then $\xi = \{\xi_1, \xi_2\}$, and we have

$$\begin{aligned} k = 0: & T_{0,0}(\xi) = T_0(\xi_1)T_0(\xi_2) = 1 \\ k = 1: & T_{1,0}(\xi) = T_1(\xi_1)T_0(\xi_2) = \xi_1, \quad L_{0,1}(\xi) = T_0(\xi_1)T_1(\xi_2) = \xi_2, \\ k = 2: & T_{2,0}(\xi) = T_2(\xi_1)T_0(\xi_2) = 2\xi_1^2 - 1, \quad T_{1,1}(\xi) = T_1(\xi_1)T_1(\xi_2) = \xi_1\xi_2, \\ & T_{0,2}(\xi) = T_0(\xi_1)T_2(\xi_2) = 2\xi_2^2 - 1 \\ & \dots \end{aligned} \tag{2}$$

A Chebyshev orthogonal polynomial of order p is used to approximate the multi-dimensional continuous function $f(\xi_1, \dots, \xi_n) : \mathfrak{R}^n \rightarrow \mathfrak{R}$, which can be expressed as follows:

$$f(\xi) \approx \sum_{i_1 + \dots + i_n \leq p} c_{i_1, \dots, i_n} T_{i_1, \dots, i_n}(\xi) = \sum_{i_1 + \dots + i_n = 0} c_{i_1, \dots, i_n} T_{i_1, \dots, i_n}(\xi) + \sum_{i_1 + \dots + i_n = 1} c_{i_1, \dots, i_n} T_{i_1, \dots, i_n}(\xi) + \dots + \sum_{i_1 + \dots + i_n = p} c_{i_1, \dots, i_n} T_{i_1, \dots, i_n}(\xi) \tag{3}$$

where N_c is the total number of undetermined coefficients, which is given by the following equation:

$$N_c = 1 + \frac{n!}{(n-1)!} + \frac{(n+1)!}{(n-1)!2!} + \frac{(n+2)!}{(n-1)!3!} + \dots + \frac{(n-1+p)!}{(n-1)!p!} = \frac{(n+p)!}{n!p!} \tag{4}$$

This weight function serves to guarantee that Chebyshev polynomials of varying orders remain orthogonal over the specified interval. For the standard Chebyshev polynomials, the weight function is expressed as follows:

$$\mathcal{W}(\xi) = \frac{1}{\sqrt{1-\xi_1^2} \cdots \sqrt{1-\xi_n^2}} \tag{5}$$

Multiplying both sides of Equation (3) by $T_{i_1, \dots, i_n}(\xi)$ and integrating the weight function $\mathcal{W}(\xi)$, the following results can be obtained:

$$\int_{-1}^1 \cdots \int_{-1}^1 T_I(\xi) T_J(\xi) \mathcal{W}(\xi) d\xi_1 \cdots d\xi_n = \begin{cases} \left(\frac{1}{2}\right)^l \pi^n & I = J \\ 0 & I \neq J \end{cases} \tag{6}$$

where l is the number of non-zeroes in i_1, \dots, i_n . The undetermined coefficients in Equation (3) can be formulated as

$$c_{i_1, \dots, i_n} = \frac{2^l}{\pi^n} \int_{-1}^1 \cdots \int_{-1}^1 f(\xi) T_{i_1, \dots, i_n}(\xi) \mathcal{W}(\xi) d\xi_1 \cdots d\xi_n \tag{7}$$

When the dimension n is small ($n \leq 5$), the coefficient in Equation (7) can be calculated by full factor numerical integration, and the calculation formula is as follows:

$$c_{i_1, \dots, i_n} \approx \frac{2^l}{\pi^n} \sum_{j_1=1}^q \cdots \sum_{j_n=1}^q f(\xi_1^{(j_1)}, \dots, \xi_n^{(j_n)}) (w_1^{(j_1)} \cdots w_n^{(j_n)}) \tag{8}$$

where $\xi_1^{(j_1)}, \dots, \xi_n^{(j_n)}$ is integration node, and q is the number of integration nodes in each dimension.

2.2. Sparse Grid Numerical Integration

In Equation (8), if the number of nodes taken for each dimensional random variable is the same and equal to q , then the total number of function evaluations required is q^n . This approach for calculating c_{i_1, \dots, i_n} is referred to as full-tensor-product grid (FTG). Regarding the selection of the number of nodes q (usually $q > 3$) in each dimension, a larger q results in higher accuracy; however, it also leads to an increase in computational workload. Consequently, when the dimension n exceeds 5, the strategy encounters a significant issue known as the “curse of dimensionality”. To alleviate this issue, an efficient approach to computing high-dimensional integrals is to use numerical integration with sparse-grid (SG) technology. The sparse grid numerical integration, also known as the sparse tensor product grid, was first proposed by Smolyak [24] and has been widely used by researchers to address high-dimensional integration problems, thereby improving the efficiency of integration. The SG with accuracy level L and n -dimensional integration is denoted as $\mathcal{G}(L, n)$, and its construction formula is as follows:

$$\mathcal{G}(L, n) = \bigcup_{\max(n, L+1) \leq \|k\|_1 \leq L+n} \bigotimes_{i=1}^n U_1^{k_i} \tag{9}$$

where $\|k\|_1 = \sum_{i=1}^n k_i$ ($k_i \geq 1$) is the 1-norm of k , and k_i is a positive integer that determines the number of integration nodes assigned to each dimensional random variable. The accuracy level L is defined as $q = L + 1$. $U_1^{k_i}$ represents a univariate quadrature rule with k_i integral nodes. The SG decomposes the direct tensor product into different sub-tensor products, using only the sub-tensor products corresponding to multi-indices that satisfy $\max(n, L + 1) \leq \|k\|_1 \leq L + n$. For example, if $n = 2$ and $L = 2$, the required multi-indices are $k = \{(1,2), (1,3), (2,1), (2,2), (3,1)\}$, and the construction of the corresponding sparse grid $\mathcal{G}(2,2)$ is given in Figure 1.

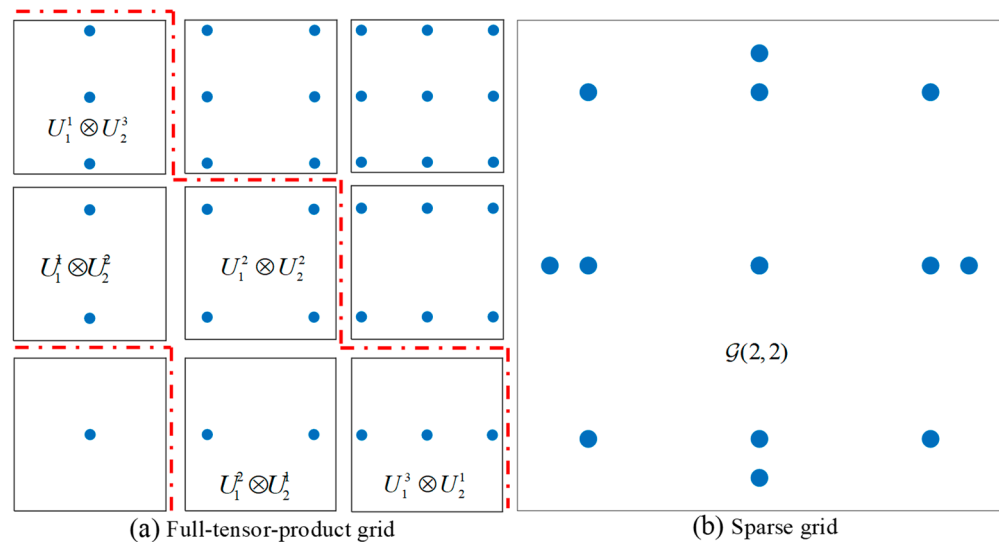


Figure 1. Schematic diagram of the construction of a sparse grid.

In Figure 1, the dots represent integration nodes; each square box represents a $[-1,1]^2$ space. The Gauss–Chebyshev integration points are used for each one-dimensional integration node, and the sub-grid corresponding to the multi-exponential k that satisfies the requirement is between the two dot–dash lines. Note that the tensor product results for sub-grids $U_1^1 \otimes U_2^3$ and $U_1^3 \otimes U_2^1$ in Figure 1a have one identical integration node, and the corresponding number of FTG nodes is 9. However, the number of integral nodes of

$\mathcal{G}(2,2)$ in Figure 1b is 13. In lower-dimensional cases ($n = 2$), achieving the same integration accuracy ($L = 2$) requires more integration nodes for the SG method, compared to the FTG method ($13 > 9$). This discrepancy arises because SG techniques are specifically designed for high-dimensional problems (typically $n > 5$). Table 1 presents the number of integration nodes required for both SG and FTG methods, corresponding to different dimensions and accuracy requirements.

Table 1. Comparison of the number of integration nodes for SG and FTG.

n	L	SG	FTG	L	SG	FTG
5	1	11	32	2	66	243
7	1	15	128	2	113	2187
10	1	21	1024	2	231	59,049
13	1	27	8192	2	243	1,594,323

Table 1 demonstrates that as dimensionality increases, the number of integration nodes required for the FTG method rises rapidly, while the growth rate of required nodes in the SG method is significantly slower. This results in a substantial reduction in the number of integration nodes compared to the full-grid method, effectively alleviating the “curse of dimensionality”.

SG numerical integration is constructed from tensor products of hierarchical difference sets based on a one-dimensional product rule. The formula for integration based on the constructed sparse grid $\mathcal{G}(L, n)$ is as follows:

$$\mathcal{G}(L, n)[f] = \sum_{\max(n, L+1) \leq \|k\|_1 \leq L+n} b(\|k\|_1) \cdot (U_1^{k_1} \otimes \dots \otimes U_1^{k_n})[f] \tag{10}$$

where f is an n -dimensional ($n > 1$) continuous function, $U_1^{k_i}(U_1^0 = 0)$ is one-dimensional product rule, and coefficient $b(\|k\|_1)$ is given by

$$b(\|k\|_1) (-1)^{L+n-\|k\|_1} \binom{n-1}{L+n-\|k\|_1} \tag{11}$$

Assuming that the number of n -dimensional SG integration nodes is N , denoted as $\mathcal{G}(L, n) = \{l_1, \dots, l_i, \dots, l_N\}$, and the weight corresponding to the i th n -dimensional integration node l_i is represented as w_i , Equation (10) can be simplified to the following form:

$$\mathcal{G}(L, n)[f] = \sum_{i=1}^N f(l_i) \cdot w_i \tag{12}$$

The weight w_i is calculated by the following equation:

$$w_i = (-1)^{L+n-\|k_i\|_1} \binom{n-1}{L+n-\|k_i\|_1} (w_1^{(i)} \dots w_n^{(i)}) \tag{13}$$

where $w_1^{(i)} \dots w_n^{(i)}$ represents the product of the corresponding weights of each one-dimensional integration node in the i th dimensional sparse-grid integration node.

2.3. Uncertainty Analysis Flow Based on Chebyshev Orthogonal Polynomials

The process of interval uncertainty analysis using Chebyshev orthogonal polynomials consists of four primary steps. First, the random variables are specified, and one-dimensional interpolation points are generated using Gauss integration nodes. These nodes serve as the foundation for the subsequent steps in the analysis. Second, n -dimensional interpolation points are created from each one-dimensional point using either the tensor product or sparse-grid integration method. The choice between these two methods de-

depends on the complexity of the problem and the desired balance between accuracy and computational efficiency. Once the n -dimensional interpolation points are established, the system response is calculated at each point, providing a comprehensive set of data for the uncertainty analysis.

In the third step, the coefficients of the Chebyshev orthogonal polynomials are computed to construct an orthogonal polynomial approximation model. This model serves as a surrogate for the original system, allowing for a more efficient uncertainty analysis. Finally, the steady-state response bounds of the rotor systems are calculated using the constructed approximation model. Once the Chebyshev orthogonal polynomial approximation is established, it can be used as a proxy model for the system, enabling efficient and accurate estimation of the steady-state response bounds through random sampling of the standard random variables using the MCS approach. Compared to the original finite element model, the use of Chebyshev orthogonal polynomials significantly enhances the efficiency of uncertainty analysis by reducing the computational burden while maintaining a high level of accuracy. Figure 2 provides a visual representation of this procedure, illustrating the flow of data and the key steps involved in the interval uncertainty analysis using Chebyshev orthogonal polynomials, thereby facilitating a clearer understanding of the methodology employed.

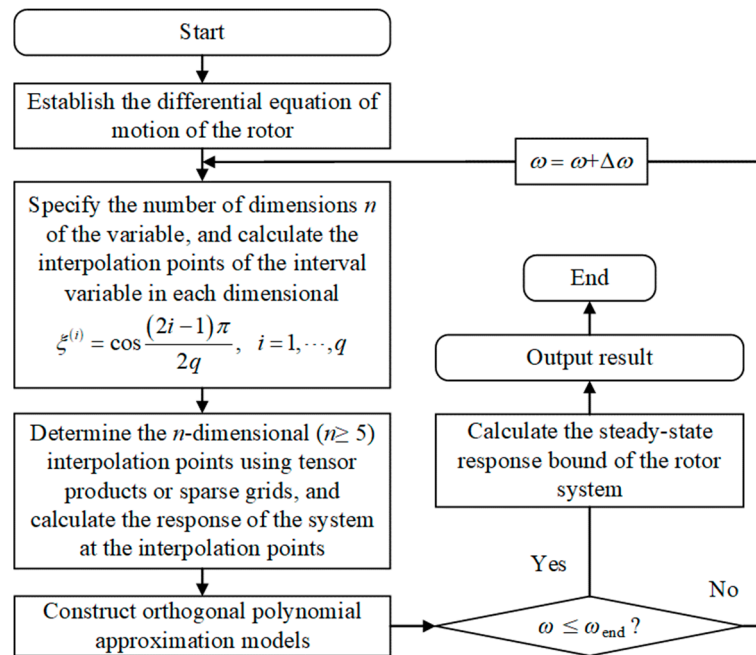


Figure 2. Uncertainty analysis procedure for the steady-state response of rotor systems by Chebyshev orthogonal polynomials.

The accuracy and predictive quality of the Chebyshev orthogonal polynomial surrogate model can be assessed using the relative generalization error, denoted as ϵ_r . The formula for calculating ϵ_r is as follows:

$$\epsilon_r = \frac{E \left[\left(\mathcal{M}(\mathcal{X}_{\text{val}}) - \mathcal{M}_{\text{Cheby}}(\mathcal{X}_{\text{val}}) \right)^2 \right]}{\text{Var}[\mathcal{M}(\mathcal{X}_{\text{val}})]} \quad (14)$$

where $E[\cdot]$ denotes the expectation operator, while $\text{Var}[\cdot]$ represents the variance operator. \mathcal{M} represents the finite element model of the rotor system (also referred to as the original model or source model), $\mathcal{M}_{\text{Cheby}}$ denotes the Chebyshev orthogonal polynomial, and \mathcal{X}_{val} represents the random validation set.

3. Rotor System

Figure 3 illustrates the dynamics similarity tester for a turboshaft engine rotor with the discs and shafts constructed from the same material (40CrMnSiA), which has an elastic modulus of 2.11×10^{11} N/m². The shaft has a length of 2.4 m and a diameter of 0.17 m. The masses of Disc 1, Disc 2, and Disc 3 are 3.3 kg, 5.83 kg, and 3.09 kg, respectively, with corresponding moments of inertia of 0.0079 kg·m², 0.0247 kg·m², and 0.0088 kg·m². The damping coefficient is 200 Ns/m. Other relevant model parameters include support stiffness, unbalanced mass on each disc, and installation phase angles. The installation phase angle of the unbalanced mass denotes the angular positions of each disc at the time of installation. The arrangement of these phase angles directly impacts the relative positioning of the unbalanced masses, thereby influencing the system's vibration patterns and stability. Specific values and interpretations of these parameters in the example rotor system are presented in Table 2.

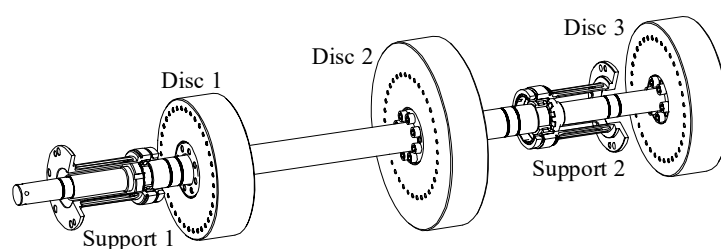


Figure 3. The structure of the rotor system.

Table 2. Model parameters.

Parameters	Dimension	Description
k_1	2.46×10^5 N/m	Stiffness of Support 1
k_2	3.64×10^5 N/m	Stiffness of Support 2
u_1	30 g·cm	Mass unbalance on Disc 1
u_2	30 g·cm	Mass unbalance on Disc 2
u_3	30 g·cm	Mass unbalance on Disc 3
ϕ_1	0°	Phase angle of unbalanced mass on Disc 2 relative to Disc 1
ϕ_2	0°	Phase angle of unbalanced mass on Disc 3 relative to Disc 1

The steady-state response of the rotor system is computed using the finite element method (FEM). For clarity, the detailed modeling process is presented in Appendix A, ensuring that the organization of this paper remains coherent. Using the established FEM, the first three critical speeds are identified as 1434 rpm, 1964 rpm, and 6923 rpm. The corresponding vibration mode shapes are depicted in Figure 4, in which the first and second modes represent pitching, while the third mode represents bending. Taking the steady-state response associated with Disc 1 as an example, the frequency response function for Disc 1 is obtained, as illustrated in Figure 5.

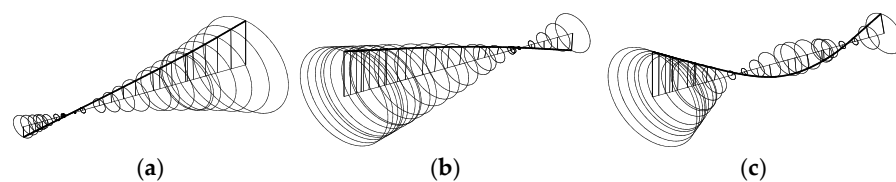


Figure 4. The first three vibration mode shapes of the example rotor: (a) 1st mode shape, (b) 2nd mode shape, and (c) 3rd mode shape.

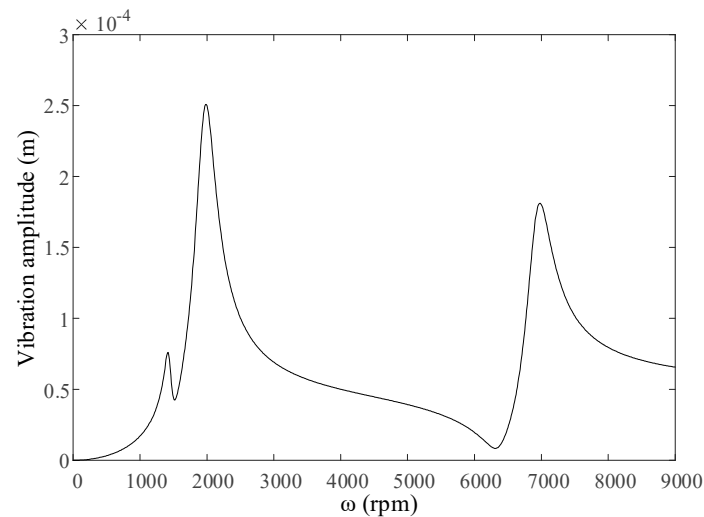


Figure 5. The steady–state unbalance response for Disc 1.

4. Numerical Results

In this section, the effects of various uncertainty parameters, including support stiffness, unbalance, and phase, as well as their combinations, are investigated with respect to their relationship to the steady-state response of the rotor system, using the method proposed in this paper. The range of response variation is obtained and compared with the results calculated through the MCS method.

4.1. Effect of Interval Support Stiffness

Assuming the degree of uncertainty is β_{K_b} , the support stiffness can be expressed in interval form as follows:

$$[\underline{K}_b, \overline{K}_b] = [K_b - \beta_{K_b} K_b, K_b + \beta_{K_b} K_b] \quad (15)$$

where K_b is the nominal value of stiffness in Support 1 or Support 2.

Generally, support stiffness comprises three components: the support structure stiffness, the squeeze film damper stiffness, and the bearing stiffness; all of these vary with temperatures, assembly states, and loads [25]. Furthermore, squirrel-cage elastic supports are widely used in jet engines, and unexpected breakage of the cage bars further increases the uncertainty of the support stiffness. Consequently, defining the precise value of support stiffness is challenging. Here, uncertain degrees of 5%, 10%, and 15% for support stiffness are considered, and uncertainty analysis is performed for these three scenarios to determine the range of steady-state responses of the rotor system. The convergence results of the relative generalization error ε_r are shown in Figure 6.

As shown in Figure 6, the error ε_r converges when the Chebyshev orthogonal polynomial is of order 3 ($p = 3$). Therefore, a third-order polynomial with four integration points in each dimension is employed. Utilizing full factorial numerical integration requires 16 invocations of the system evaluation model. The results of the uncertainty analysis for the steady-state response of Disc 1 are presented in Figure 7.

As shown in Figure 7, near the critical speed, the range of vibration amplitude broadens as the degrees of uncertainty increase. This phenomenon is more pronounced at the first and second critical speeds compared to the third, indicating that the dynamic response at these speeds is more sensitive to changes in support stiffness. In the range from 1000 to 4000 rpm, the resonance frequency, initially characterized by a single-peak mode, transitions into a broad resonance band. At the upper bound, the distinction between the first and second order becomes very blurred. The steady-state response exhibits less variability when the rotational speed exceeds 4000 rpm.

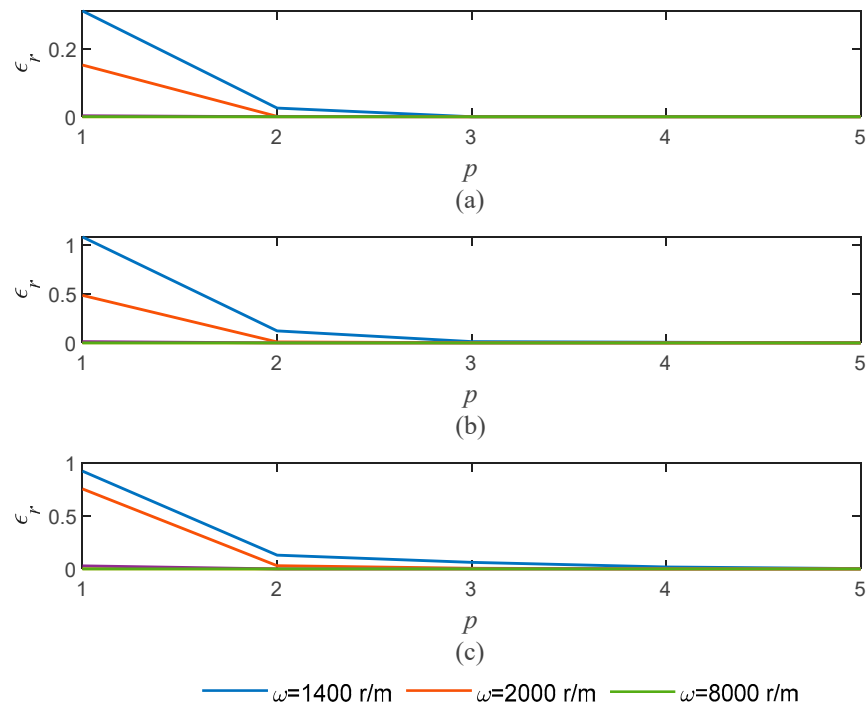


Figure 6. Convergence analysis of ϵ_r under varying degrees of uncertainty in support stiffness. (a) 5% (b) 10% (c) 15%.

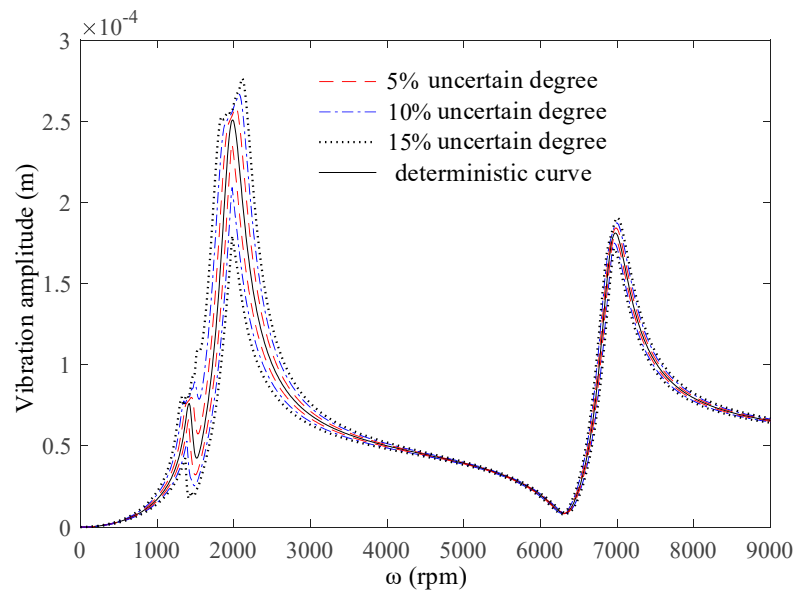


Figure 7. Dynamic response range of Disc 1, with intervals of support stiffness.

4.2. Effect of Interval Mass Unbalance

Unbalance in a rotor is unavoidable, due to manufacturing and assembly errors. The mass unbalance is considered as an interval variable, one expressed in the following form:

$$[e, \bar{e}] = [e - \beta_e e, e + \beta_e e] \tag{16}$$

where e is the nominal value (30 g·cm) of mass unbalance in Discs 1, 2, and 3, and β_e is the degree of uncertainty. The steady-state response of the rotor system is calculated for uncertainty degrees of 5%, 10%, and 15%, respectively. Similar to the convergence analysis described in Section 4.1, a third-order ($p = 3$) Chebyshev orthogonal polynomial with four

Gaussian integration nodes in each dimension has been constructed. The variation in the steady-state response of Disc 1 is shown in Figure 8.

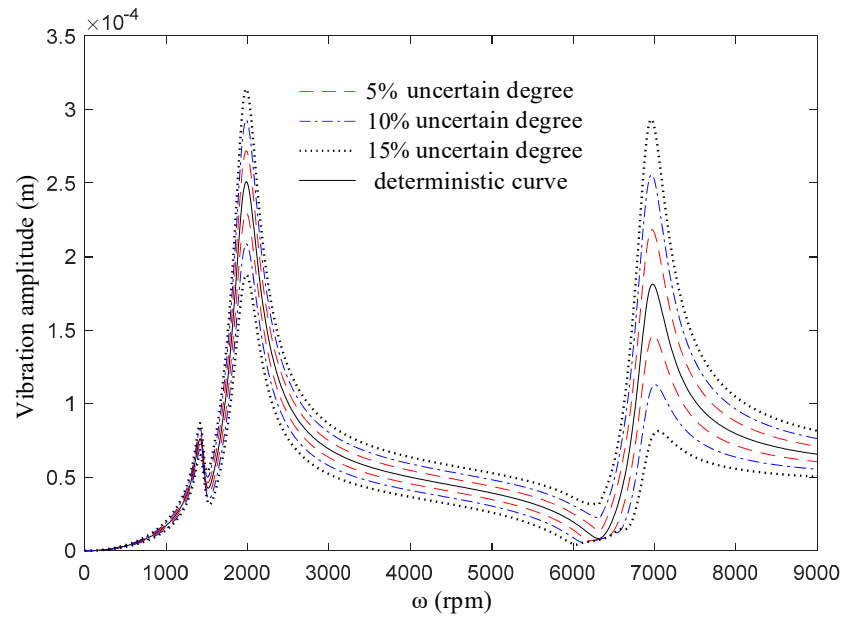


Figure 8. Dynamic response range of Disc 1, with intervals of mass unbalance.

Figure 8 illustrates that the range of steady-state amplitude widens as the rotational speed increases, indicating that higher rotational speeds amplify the effect of mass unbalance uncertainty on the vibration amplitude of the rotor system. Additionally, the upper and lower bounds are symmetric about the deterministic curve, while the critical speed remains unchanged.

4.3. Effect of Interval Unbalance Phase

Taking the unbalance phase of Disc 1 as a reference and assuming that the unbalance phase of Disc 1 is 0° , the unbalance phase shifts of Discs 2 and 3 fluctuate within the range of $[0, 360^\circ]$. The convergence results of the relative error at different speeds are presented in Figure 9.

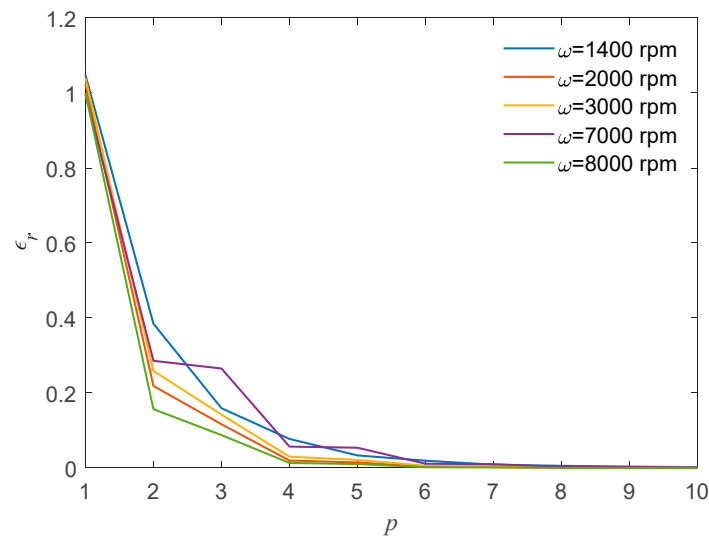


Figure 9. Convergence analysis of posterior error in chaotic polynomials due to phase angle uncertainty.

As shown in Figure 9, to consider the convergence of the relative error, a Chebyshev orthogonal polynomial of order ($p = 8$) is constructed. This forms the basis for conducting an uncertainty propagation analysis of the phase angle of the mass imbalance across the entire speed range. Figure 10 illustrates the variation range of the steady-state response at Disc 1.

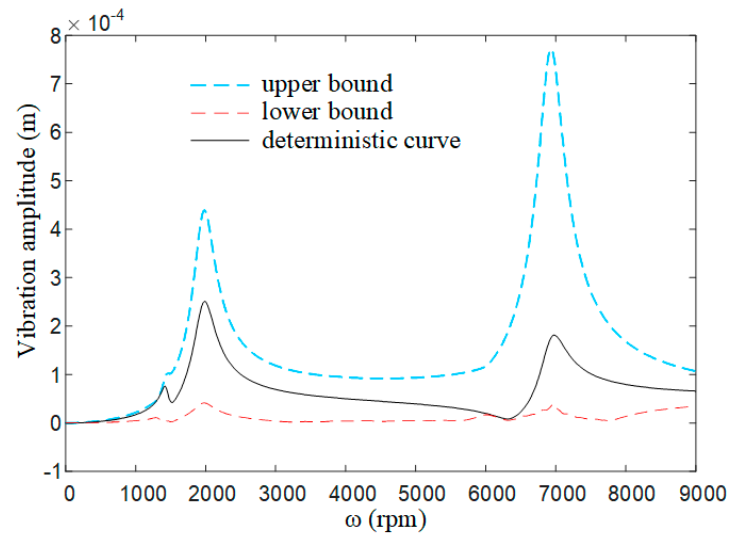


Figure 10. Steady–state response range of disk 1 under uncertain imbalanced phase.

As shown in Figure 10, uncertainty in the unbalance phase significantly impacts the steady-state response of the rotor, particularly at the third-order critical speed, at which the maximum amplitude increases by nearly threefold compared to the deterministic case. Changes in the unbalance phase alter the direction of the corresponding centrifugal force, consequently modifying the total centrifugal force on the rotor and the force couples. To ensure that the rotor operates reliably and safely, it is essential to account for the uncertainty of the unbalance phase during the design and assembly process, thereby preventing excessive unbalance-phase differences between the discs due to oversight.

4.4. Effect of Multi Interval Parameters

In practice, the uncertain parameters affecting rotor performance are typically diverse. This subsection investigates the simultaneous effects of seven uncertainty parameters—namely, interval stiffness in supports 1 and 2, interval mass unbalance in Discs 1, 2, and 3, and interval unbalance phase in Discs 2 and 3—on the rotor’s steady-state response. The degrees of uncertainty for stiffness and mass unbalance are assumed to be 5%, 10%, and 15%, respectively. Given the significant impact of phase fluctuations on vibration, only the scenario where the phase angle varies within $\pm 5^\circ$ is considered, with the phase of Disc 1 fixed as a reference. Three cases are established based on the degrees of uncertainty for all parameters, and uncertainty analysis is conducted for these scenarios. For clarity, the degrees of uncertainty for all parameters are summarized in Table 3.

Table 3. The degrees of uncertainty for all parameters.

Parameters	Degrees of Uncertainty		
	Case 1	Case 2	Case 3
k_1	5%	10%	15%
k_2	5%	10%	15%
u_1	5%	10%	15%
u_2	5%	10%	15%
u_3	5%	10%	15%
ϕ_1	$\pm 5^\circ$	$\pm 5^\circ$	$\pm 5^\circ$
ϕ_2	$\pm 5^\circ$	$\pm 5^\circ$	$\pm 5^\circ$

When the Chebyshev orthogonal polynomial is of order 3 ($p = 3$), the relative error ε_r achieves convergence. Consequently, a third-order Chebyshev orthogonal polynomial is utilized to calculate the range of steady-state response variations of the system under multiple sources of uncertainty and varying parameter intervals. The range of steady-state response for Disc 1, obtained using the proposed method, is illustrated in Figure 11.

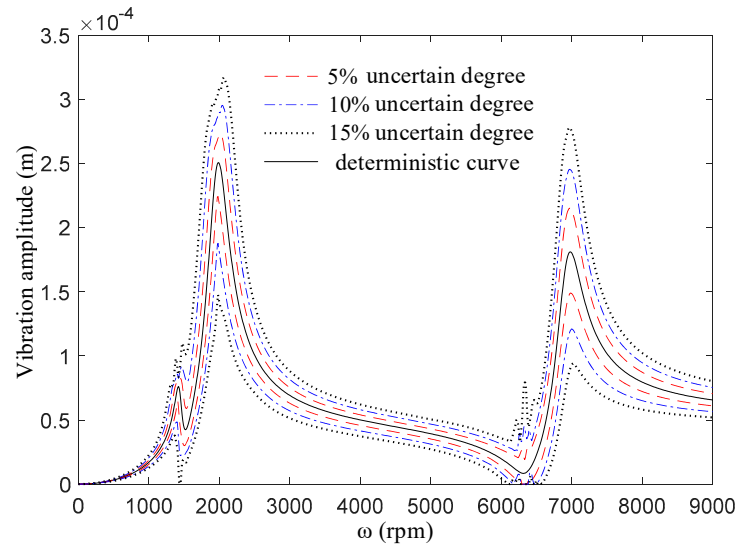


Figure 11. Steady–state response variation of Disc 1 under multiple uncertain parameters.

As shown in Figure 11, having multiple uncertainty parameters significantly affects the steady-state response of the rotor. This pattern of influence encompasses the characteristics exhibited by the individual parameters described earlier, including broad resonance bands, peak shifts, and fluctuations in amplitude magnitude.

4.5. Comparison and Validation

To validate the correctness of the proposed method, a comparison is made using the MCS method. Since the comparison processes for different uncertainties are consistent, due to space constraints, only one scenario is analyzed here, specifically, the one in which the uncertainties in support stiffness and mass imbalance are set at 10%, while the phase angles in Discs 2 and 3 fluctuate within a range of $\pm 5^\circ$. The comparison’s results are illustrated in Figures 12 and 13.

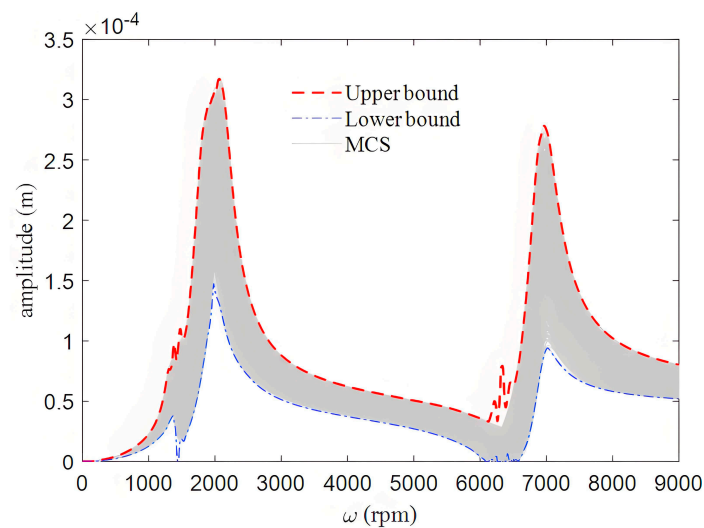


Figure 12. Comparison between the proposed method and the MCS method.

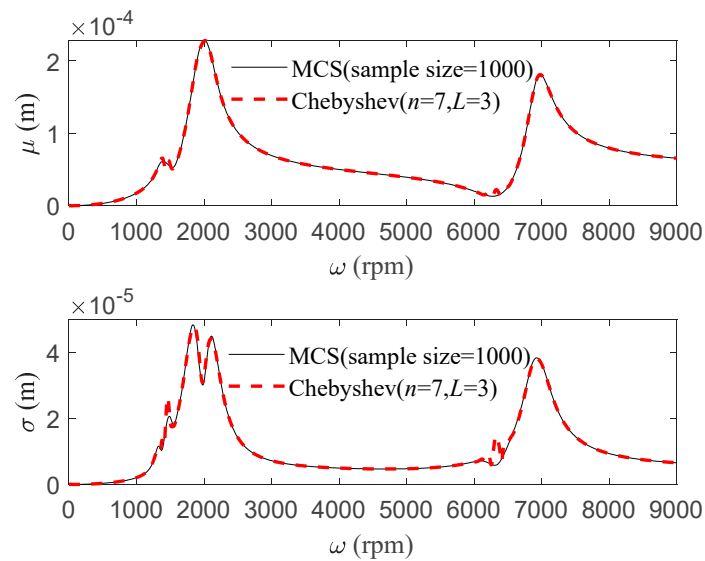


Figure 13. Comparison of mean and standard deviation of steady-state response.

In Figure 12, the random sample size used for the MCS is 1000, and L in Figure 13 is the accuracy level of the sparse-grid integration used for establishing the Chebyshev orthogonal polynomial. The results indicate that the envelope intervals obtained by the two methods coincide, except at the anti-resonance point near 6500 rpm. Additionally, the statistical means and standard deviations of the steady-state responses obtained by both methods are nearly identical, which verifies the accuracy of the method proposed in this paper under conditions of multiple uncertainties. Table 4 presents a comparison of the computational efficiency of the MCS and FTG methods and the method proposed in this paper.

Table 4. Comparison of computational efficiency.

Method	FTG Method	MCS Method	Proposed Method
Computational cost	16,384	1000	680

In Table 4, the computational cost refers to the number of times the finite element model of the rotor system is invoked during the uncertainty analysis process. For example, the FTG method, which employs a full tensor product mesh with four integration points in each dimension, requires a total of 16,384 integration nodes, necessitating 16,384 invocations of the source model. In contrast, sparse-grid numerical integration requires only 680 invocations. Furthermore, when looking at the percentage reduction in computational cost, sparse-grid integration requires only 68% of the computational cost associated with the MCS. Compared to the FTG method, sparse-grid integration reduces the computational cost by approximately 95.87%, highlighting its superiority in high-dimensional cases. Therefore, employing sparse-grid integration in high-dimensional cases can significantly enhance computational efficiency.

5. Conclusions

In this paper, the method of Chebyshev orthogonal polynomials is utilized to compute the steady-state response of a rotor with uncertainties. To enhance computational efficiency in high-dimensional scenarios involving multiple uncertain parameters, the sparse-grid numerical integration method is employed. A dynamically similar rotor of a turboshaft engine is selected as the study's subject, and the influences of multiple uncertain parameters on the rotor's dynamics are analyzed. The main conclusions are as follows:

- (1) The uncertainty in support stiffness significantly affects the steady-state response and critical speed, causing the resonance frequency, originally characterized by a single-peak pattern, to transform into a broad resonance band; this is accompanied by shifts in the resonance peak.
- (2) The upper and lower bounds of the steady-state response are symmetric around the deterministic curve under the influence of mass-unbalance uncertainty, with these bounds widening at high rotational speeds, although the critical speed remains unchanged. Additionally, the phase of the uncertainty unbalance significantly influences the dynamic response of the rotor, resulting in substantial increases in vibration amplitude at critical speeds.
- (3) The effects of multiple uncertainty parameters together on the rotor's steady-state response are multifaceted, characterized by broad amplitude bands, resonance peaks, frequency shifts, and fluctuations in amplitude magnitude.

In summary, the method proposed in this paper integrates Chebyshev orthogonal polynomial approximation with sparse-grid numerical integration techniques, targeting the analysis of high-dimensional random variables. By utilizing sparse-grid integration, the approach addresses the computational challenges associated with the “curse of dimensionality”, allowing for efficient processing without compromising accuracy. The combination of these techniques not only streamlines the computation but also enhances the robustness of the results, making it a valuable method for engineers and researchers dealing with high-dimensional problems in rotor dynamics and related fields.

Future research will concentrate on the experimental validation of uncertainties in rotor systems to enhance the connections between theoretical models and practical applications. Systematic experimental protocols will be developed to elucidate how various uncertainty factors influence rotor dynamic performance, thereby providing empirical evidence to confirm the accuracy of these models. Furthermore, a strong emphasis on robust optimization methods is crucial, as it integrates results from uncertainty analysis to create designs that are both efficient and resilient to variations in operational conditions.

Author Contributions: Writing—review and editing, software, B.X.; writing—original draft preparation, P.N.; visualization, G.W.; supervision, C.Z. All authors have read and agreed to the published version of the manuscript.

Funding: This research was funded by [National Natural Science Foundation of China] grant number [No. 52366002], [Project on Enhancement of Basic Research Ability of Young and Middle-Aged Teachers in Guangxi's Universities] grant number [No. 2023KY0827], and [GUAT Special Research Project on the Strategic Development of Distinctive Interdisciplinary Fields] grant number [No.TS2024411].

Institutional Review Board Statement: Not applicable.

Informed Consent Statement: Not applicable.

Data Availability Statement: The data presented in this study are available in the article.

Conflicts of Interest: The authors declare no conflict of interest.

Appendix A

A schematic representation of the finite element model established for the rotor system is shown in Figure A1.

In Figure A1, the shaft of the rotor system is modeled using one-dimensional Timoshenko beam elements, divided into 25 segments. The discs are represented by concentrated mass elements, while the red triangles indicate the bearing elements. “Brg Type 3” specifies that the bearing has constant stiffness and damping, and no rotational stiffness. The load–deformation relationship of the bearing is typically nonlinear and closely related to the rotational speed. To simplify the rotor dynamic analysis, the load–deformation relationship of the supports is often approximated as linear.

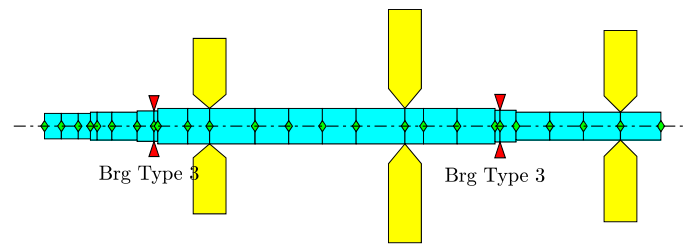


Figure A1. The established FEM of the rotor System.

Considering only the lateral bending vibration, the shaft beam element can be described by 8 degrees of freedom. The analysis of beam bending can be approached similarly to that of bar extension. Figure A2 shows a typical element, along with its local coordinates. To guarantee the continuity of both deflection and slope at the element boundaries, the local coordinates incorporate the translations and rotations at the ends of the element.

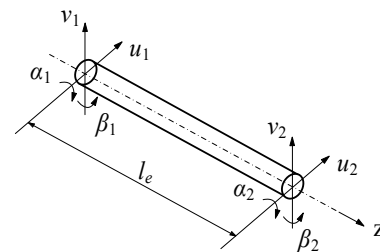


Figure A2. Degrees of freedom of axis elements and nodes.

In Figure A2, l_e is the length of the axis unit, and each node has four degrees of freedom, which, respectively, represent the node displacement along the x and y directions (represented by u and v respectively) and the cross-sectional rotation around the x and y axes (represented by $\alpha = v/z$ and $\beta = u/z$ respectively). Therefore, eight coordinate components are needed to describe the displacement x_e of the shaft unit, namely

$$x_e = [u_1 v_1 \alpha_1 \beta_1 u_2 v_2 \alpha_2 \beta_2]^T \tag{A1}$$

The shaft element model is given by the following formula:

$$M_e \ddot{x}_e + (C_e + \omega G_e) \{\dot{x}_e\} + K_e x_e = q_e \tag{A2}$$

where the vector q_e is the force applied to each node on the shaft unit, and ω is the rotational speed of the rotor. M_e , G_e , K_e , and C_e are the mass matrix, gyro matrix, stiffness matrix, and damping matrix of the shaft element, respectively. The density, cross-sectional area, elastic modulus, and moment of inertia of the shaft element are, respectively, denoted as ρ_e , A_e , E_e , and I_e , and the specific forms of the element matrices M_e , G_e , and K_e are as follows:

$$M_e = \frac{\rho_e A_e l_e}{420} \begin{bmatrix} 156 & 0 & 0 & 22l_e & 54 & 0 & 0 & -13l_e \\ 0 & 156 & -22l_e & 0 & 0 & 54 & 13l_e & 0 \\ 0 & -22l_e & 4l_e & 0 & 0 & -13l_e & -3l_e^2 & 0 \\ 22l_e & 0 & 0 & 4l_e^2 & 13l_e & 0 & 0 & -3l_e^2 \\ 54 & 0 & 0 & 13l_e & 156 & 0 & 0 & -22l_e \\ 0 & 54 & -13l_e & 0 & 0 & 156 & 22l_e & 0 \\ 0 & 13l_e & -3l_e^2 & 0 & 0 & 22l_e & 4l_e^2 & 0 \\ -13l_e & 0 & 0 & -3l_e^2 & -22l_e & 0 & 0 & 4l_e^2 \end{bmatrix} \tag{A3}$$

$$K_e = \frac{E_e I_e}{l_e^3} \begin{bmatrix} 12 & 0 & 0 & 6l_e & -12 & 0 & 0 & 6l_e \\ 0 & 12 & -6l_e & 0 & 0 & -12 & -6l_e & 0 \\ 0 & -6l_e & 4l_e^2 & 0 & 0 & 6l_e & 2l_e^2 & 0 \\ 6l_e & 0 & 0 & 4l_e^2 & -6l_e & 0 & 0 & 2l_e^2 \\ -12 & 0 & 0 & -6l_e & 12 & 0 & 0 & -6l_e \\ 0 & -12 & 6l_e & 0 & 0 & 12 & 6l_e & 0 \\ 0 & -6l_e & 2l_e^2 & 0 & 0 & 6l_e & 4l_e^2 & 0 \\ 6l_e & 0 & 0 & 2l_e^2 & -6l_e & 0 & 0 & 4l_e^2 \end{bmatrix} \tag{A4}$$

$$G_e = \frac{\rho_e I_e}{15l_e} \begin{bmatrix} 0 & 36 & -3l_e & 0 & 0 & -36 & -3l_e & 0 \\ -36 & 0 & 0 & -3l_e & 36 & 0 & 0 & -3l_e \\ 3l_e & 0 & 0 & 4l_e^2 & -3l_e & 0 & 0 & -l_e^2 \\ 0 & 3l_e & -4l_e^2 & 0 & 0 & -3l_e & l_e^2 & 0 \\ 0 & -36 & 3l_e & 0 & 0 & 36 & 3l_e & 0 \\ 36 & 0 & 0 & 3l_e & -36 & 0 & 0 & 3l_e \\ 3l_e & 0 & 0 & -l_e^2 & -3l_e & 0 & 0 & 4l_e^2 \\ 0 & 3l_e & l_e^2 & 0 & 0 & -3l_e & -4l_e^2 & 0 \end{bmatrix} \tag{A5}$$

Considering the rigid disc as a concentrated mass on the node of the shaft unit can effectively reduce the degree of freedom of the model and improve the calculation efficiency of the finite element model. The model of the rigid disc is given by the following formula:

$$M_d \ddot{x}_d + \omega G_d \dot{x}_d = q_d \tag{A6}$$

where the vector q_d is the unbalanced force caused by eccentric mass, M_d and G_d are the mass matrix and gyro matrix of the disc, and

$$M_d = \begin{bmatrix} m_d & 0 & 0 & 0 \\ 0 & m_d & 0 & 0 \\ 0 & 0 & I_d & 0 \\ 0 & 0 & 0 & I_d \end{bmatrix} \tag{A7}$$

$$G_d = \begin{bmatrix} 0 & 0 & 0 & 0 \\ 0 & 0 & 0 & 0 \\ 0 & 0 & 0 & I_p \\ 0 & 0 & I_p & 0 \end{bmatrix} \tag{A8}$$

where m_d is the mass of the disc, I_d is the diameter moment of inertia, and I_p is the polar moment of inertia.

In Equation (A6), the unbalanced force q_d is given by the following equation:

$$q_d = [m_e d_e \omega^2 \cos(\omega t + \phi) \ m_e d_e \omega^2 \sin(\omega t + \phi) \ 0 \ 0]^T \tag{A9}$$

where m_e and d_e are the magnitude of unbalance and eccentricity, and ϕ represents the initial angular positions of unbalance, as shown in Figure A3.

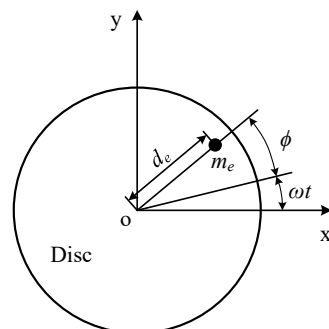


Figure A3. Schematic diagram of mass unbalance.

Based on finite element theory, the general process for constructing the differential equation of the rotor system is as follows: (1) Assemble the element mass, stiffness, damping, and gyroscopic matrices into a global matrix. (2) Incorporate supports and constraints. (3) Apply external excitation. The resulting differential equation of motion for the entire rotor system can then be expressed in the following form:

$$M\ddot{x} + (C + \omega G)\dot{x} + (K + K_b)x = q \quad (\text{A10})$$

where x is the node displacement, ω is the rotor speed, and M , C , K , and G are the overall mass matrix, damping matrix, stiffness matrix, and gyro matrix of the rotor system. K_b is the supporting stiffness matrix, and q is the unbalanced force acting on the whole rotor system. Considering that the unbalanced force can be written as $q = Qe^{i\omega t}$, the response vector can be written as $x = Xe^{i\omega t}$, where X is the amplitude of the unbalanced response. Transforming the motion equation of the rotor system shown in Equation (A10) into frequency domain, we have

$$Z(\omega)X(\omega) = Q(\omega) \quad (\text{A11})$$

where

$$Z(\omega) = -\omega^2 M + i\omega(C + \omega G) + K + K_b \quad (\text{A12})$$

Equation (A12) can be employed to calculate the unbalanced response at each node of the rotor system at a specified speed. The unbalanced steady-state response of the rotor at each node follows a distinct trajectory. When the supporting parameters are isotropic, the trajectory is circular, with the radius representing the amplitude of the unbalanced response in the X and Y directions at the rotor cross-section. Conversely, if the bearing parameters differ in the two directions, the trajectory takes the form of an ellipse.

References

1. Qingshan, Z.; Zhenhui, H.; Jun, H.; Shiyuan, P. Research on dynamic characteristics of aero-engine high-pressure rotor connection component loose fault. *J. Aerosp. Power* **2024**, *39*, 151–166.
2. Zhenyong, L.; Lei, H.; Shengliang, H. Dynamic characteristics of an aero-engine rotor system with crack faults. *J. Vib. Shock* **2018**, *37*, 40–46.
3. Li, Y.Q.; Luo, Z.; Li, J.; Hou, X.J. Analysis of Bolted Joint Rotor System with Uncertain Axial Stiffness. *J. Northeast. Univ. (Nat. Sci.)* **2019**, *40*, 700–704+721.
4. Xinxing, M.; Zhenguo, Z.; Hongxing, H. Nonlinear vibration responses of a rubbing rotor considering the non-probabilistic uncertainty of parameters. *J. Vib. Shock* **2021**, *40*, 56–62.
5. Yanxu, L.; Baoguo, L.; Zhen, Z.; Wei, F.; Ruifeng, Z. Nonparametric modeling and dispersion parameter identification for uncertain rotor systems. *J. Aerosp. Power* **2023**, *38*, 2527–2535.
6. Hongliang, Y.; Xiangsong, L.; Degang, W.; Wen, B. Applications of fuzzy random finite element method to rotor dynamics. *Chin. J. Appl. Mech.* **2010**, *27*, 384–387.
7. Koroishi, E.H.; Cavalini, A.A., Jr.; de Lima, A.M.; Steffen, V., Jr. Stochastic modeling of flexible rotors. *J. Braz. Soc. Mech. Sci. Eng.* **2012**, *34*, 574–583. [[CrossRef](#)]
8. Liu, Y.; Zhang, Y.; Wu, Z. Stochastic dynamic analysis of the rotor-bearing system considering the randomness of the radial clearance. *J. Braz. Soc. Mech. Sci. Eng.* **2019**, *41*, 1–13. [[CrossRef](#)]
9. Fu, C.; Ren, X.; Yang, Y.; Deng, W. Application and comparative analysis of orthogonal polynomials in uncertain rotor dynamic response calculation. *J. Aerosp. Power* **2018**, *33*, 2228–2234.
10. Lara-Molina, F.A.; Koroishi, E.H.; Steffen, V., Jr. Uncertainty analysis of flexible rotors considering fuzzy parameters and fuzzy-random parameters. *Lat. Am. J. Solids Struct.* **2015**, *12*, 1807–1823. [[CrossRef](#)]
11. Lara-Molina, F.A.; Cavalini, A.A.; Steffen, V.; Cabrera, N.V. Tilting-Pad Journal Bearing Subjected to Fuzzy Type-2 Uncertain Parameters. *J. Vib. Acoust.* **2019**, *141*, 061008.1–061008.9. [[CrossRef](#)]
12. Wu, J.; Zhang, Y.; Chen, L.; Luo, Z. A Chebyshev interval method for nonlinear dynamic systems under uncertainty. *Appl. Math. Model.* **2013**, *37*, 4578–4591. [[CrossRef](#)]
13. Fu, C.; Ren, X.; Yang, Y.; Qin, W. Dynamic response analysis of an overhung rotor with interval uncertainties. *Nonlinear Dyn.* **2017**, *89*, 2115–2124. [[CrossRef](#)]
14. Ma, Y.; Wang, Y.; Wang, C.; Hong, J. Nonlinear interval analysis of rotor response with joints under uncertainties. *Chin. J. Aeronaut.* **2020**, *33*, 205–218. [[CrossRef](#)]
15. Ma, Y.; Wang, Y.; Wang, C.; Jie, H. Interval analysis of rotor dynamic response based on Chebyshev polynomials. *Chin. J. Aeronaut.* **2020**, *33*, 2342–2356. [[CrossRef](#)]

16. Mao, W.; Zhang, N.; Feng, D.; Li, J. A Proposed Bearing Load Identification Method to Uncertain Rotor Systems. *Shock Vib.* **2021**, *13*, 6615761. [[CrossRef](#)]
17. Fu, C.; Ren, X.; Yang, Y. Vibration Analysis of Rotors Under Uncertainty Based on Legendre Series. *J. Vib. Eng. Technol.* **2019**, *7*, 43–51. [[CrossRef](#)]
18. Fu, C.; Xu, Y.; Yang, Y.; Lu, K.; Gu, F.; Ball, A. Dynamics analysis of a hollow-shaft rotor system with an open crack under model uncertainties. *Commun. Nonlinear Sci. Numer. Simul.* **2020**, *83*, 105102. [[CrossRef](#)]
19. Fu, C.; Lu, K.; Yang, Y.; Xie, Z.; Ming, A. Nonlinear Vibrations of an Uncertain Dual-Rotor Rolling Bearings System with Coupling Misalignment. *J. Nonlinear Math. Phys.* **2022**, *29*, 388–402. [[CrossRef](#)]
20. Didier, J.; Faverjon, B.; Sinou, J.J. Analysing the dynamic response of a rotor system under uncertain parameters by polynomial chaos expansion. *J. Vib. Control* **2012**, *18*, 712–732. [[CrossRef](#)]
21. Zhang, Z.; Ma, X.; Yu, H.; Hua, H. Stochastic dynamics and sensitivity analysis of a multistage marine shafting system with uncertainties. *Ocean Eng.* **2020**, *219*, 108388. [[CrossRef](#)]
22. Lasota, R.; Stocki, R.; Tazowski, P.; Szolc, T. Polynomial chaos expansion method in estimating probability distribution of rotor-shaft dynamic responses. *Bull. Pol. Acad. Sci. Tech. Sci.* **2015**, *63*, 413–422. [[CrossRef](#)]
23. Lu, K.; Yang, Y.; Xia, Y.; Fu, C. Statistical moment analysis of nonlinear rotor system with multi uncertain variables. *Mech. Syst. Signal Process.* **2019**, *116*, 1029–1041. [[CrossRef](#)]
24. Smolyak, S. Quadrature and interpolation formulas for tensor products of certain classes of functions. *Dokl. Akad. Nauk Sssr* **1963**, *4*, 1042–1045.
25. Ma, Y.; Liang, Z.; Chen, M.; Hong, J. Interval analysis of rotor dynamic response with uncertain parameters. *J. Sound Vib.* **2013**, *332*, 3869–3880. [[CrossRef](#)]

Disclaimer/Publisher’s Note: The statements, opinions and data contained in all publications are solely those of the individual author(s) and contributor(s) and not of MDPI and/or the editor(s). MDPI and/or the editor(s) disclaim responsibility for any injury to people or property resulting from any ideas, methods, instructions or products referred to in the content.